ChemPubSoc Europe

DOI: 10.1002/cssc.201403125

CHEMSUSCHEM Full Papers

GCE

Sonophotodeposition of Bimetallic Photocatalysts Pd–Au/TiO_2: Application to Selective Oxidation of Methanol to Methyl Formate

Juan C. Colmenares,* Paweł Lisowski, Dariusz Łomot, Olga Chernyayeva, and Dmytro Lisovytskiy[a]

The aim of this work is to develop bimetallic Pd–Au/TiO_2 P90 systems, which are highly active and selective for the photocatalytic oxidation of methanol to form methyl formate. Modification of commercial TiO_2 P90 with Pd–Au nanoparticles was successfully achieved for the first time by means of a sonophotodeposition (SPD) method. The prepared materials were characterized by TEM, UV/Vis spectroscopy, X-ray photoelectron spectroscopy, and powder XRD. The Pd–Au bimetallic nanoparticles supported on titania exhibited remarkably enhanced catalytic activity in selective methanol oxidation to form methyl formate due to the synergism of Au and Pd particles, as well as the strong interaction between TiO_2 and Pd–Au. SPD is a green methodology that can be used to prepare well-defined bimetallic surfaces on semiconductor supports with great promise for catalytic applications, in which selectivity can be tuned through adjustment of the surface composition.

Introduction

Heterogeneous photocatalysis is an important research topic owing to the irreplaceable role of photocatalysts in organic synthesis and the design of chemical processes that are atom-efficient. It is also an attractive technique for the complete destruction of undesirable contaminants in both the aqueous and gas phases by using solar or artificial light illumination.[1] One key aspect in photocatalysis research is to identify structure–performance relationships, which can help in improving photocatalytic performance and designing better materials. Although in the last decades, the term "photocatalyst design", which implies the preparation of photocatalysts with desired properties and a strict control of the synthetic conditions, has become widely accepted, further progress in this field is still required.

There are many merits associated with an advanced oxidation process, which is the subject of a huge number of studies related to practical applications, especially water purification and removal of indoor air pollution, in which organic and inorganic pollutants are totally degraded into innocuous substances over mainly TiO_2-based photocatalysts. The problem is especially severe for volatile organic compounds (VOCs) that have been linked to adverse health effects.[2] Titania is a benchmark material that has received tremendous attention in both industrial and environmental applications due to its good photostability, nontoxicity, and large commercial availability. However, despite these desirable properties, a poor quantum yield caused by the rapid recombination of photogenerated electrons and holes has become the bottleneck of its widespread use in practical applications.[3] Thus, numerous studies have focused on enhancing the photocatalytic activity of TiO_2 by using doping, semiconductor coupling, surface sensitization method, and so on.[4,5] Bimetallic nanoparticles, composed of two different noble-metal components, can exhibit interesting electronic, optical, and catalytic or photocatalytic properties that are absent in the corresponding monometallic nanoparticles.[6–10] The physical and chemical properties of bimetallic particles are usually different from those of their single-metal counterparts, and they vary significantly as a function of composition and particle size.[11–16] They are also expected to display not only a combination of properties associated with two distinct metals, but also new properties of surface metal sites that are strongly affected by strong metal–support interactions (SMSIs), which are characterized by electron transfer from the support to the metal and/or heteroatomic interfacial bonds; this causes significant changes to the surface chemistry and enhanced reactivity at a specific site driven by electron-transfer phenomena and (in some cases) encapsulation of the metal particles. Both metals have also shown considerable potential as heterogeneous catalysts for different selective oxidation reactions in the gas phase.[17,18]

Methanol, which is produced from natural gas, coal, and biomass, is an attractive starting material for the synthesis of various fuels and chemicals and also represents a typical VOC model compound.[2,19,20] However, there have been few studies on the selective photocatalytic oxidation of methanol over TiO_2 photocatalysts because complete oxidation occurs predominantly over TiO_2 and the selectivity of intermediate products decreases significantly.[21,22] Among diverse routes for

[a] Dr. J. C. Colmenares, P. Lisowski, Dr. D. Łomot, Dr. O. Chernyayeva, Dr. D. Lisovytskiy
Institute of Physical Chemistry PAS
Kasprzaka 44/52, 01-224 Warsaw (Poland)
E-mail: jcarloscolmenares@ichf.edu.pl

GCE This publication is part of a Special Issue on "Green Chemistry and the Environment". To view the complete issue, visit: http://onlinelibrary.wiley.com/doi/10.1002/cssc.v8.10/issuetoc

methanol conversion and utilization, the selective oxidation of methanol to form methyl formate (MF) is attractive as a simple and environmentally benign process to obtain valuable methanol-downstream products; therefore, its efficient production is of technological importance.

The industrial production of MF by the carbonylation of methanol in the presence of a strong base (e.g., sodium methoxide) has been carried out on a large scale for many years during the production of formic acid (the BASF process).[23] Most of the MF produced is used as an intermediate for the production of formic acid and formamide. DMF is produced by reacting MF with dimethylamine. A new use has been found for MF in the production of foundry molds. With the anticipated extension of C1 chemistry, MF may be used as an intermediate for a number of products.[23]

Kominami et al.[24] reported pioneering work on photocatalytic oxidation under UV irradiation of gaseous methanol to form MF on titania (anatase) in 2010. MF was obtained at room temperature with a selectivity of up to 91% and conversions between 8 and 28% (at 250 °C), whereas formaldehyde, CO, and CO_2 were detected as minor products. The authors claimed that the contact time of the gas mixture with TiO_2 was one of the key factors to obtain good selectivity and avoid deep complete oxidation of the desired product. In other studies, Guo et al. observed the formation of MF on TiO_2 under light irradiation at $\lambda = 400$ nm,[25] whereas Phillips et al. demonstrated two consecutive photo-oxidation steps that led to MF from methanol by studying the reaction mechanism using mass spectrometry and scanning tunneling microscopy.[26] Yang et al. reported that Au–Ag alloy nanoparticles supported on titania exhibited very high methanol conversion (>90%) and MF selectivity (>85%) for the selective oxidation of methanol by using a low partial pressure of oxygen in air under UV irradiation in the 15–45 °C temperature range.[27] The photocatalytic process becomes a new route to the production of MF from methanol.

In the context of photocatalytic synthesis, traditional methods of noble-metal deposition on solid catalysts usually require several steps and invariably imply the loss of a certain fraction of noble metal. Recently, more and more attention has been paid to the use of ultrasound (US) irradiation in the preparation of photocatalysts.[10,28] During US irradiation, bubbles in solution are implosively collapsed by acoustic fields, and high-temperature (≈5000 °C) and high-pressure fields (≈1800 atm; 1 atm = 101325 Pa) are produced at the centers of the collapsing bubbles. This effect is known as acoustic cavitation. US activation, which is found in cavitation effects leading to mass transfer development, is extensively used nowadays to promote synthetic materials chemistry and also preparation of photocatalysts.[29] US provides rather unusual reaction conditions (rapid formation of extremely high temperatures and pressures in liquids) that cannot be realized by other methods, and in which high-energy chemical reactions can occur. The chemical effect of US operation in liquids is the formation of free radicals, for example, $^{\bullet}H$ and $^{\bullet}OH$. Then, they can recombine to form H_2O or interact to form H_2, H_2O_2, or $^{\bullet}HO_2$. These radicals and compounds, with strong oxidative and reductive properties, are sources of various sonochemical processes in aqueous solutions.

We recently showed that very active monometallic titanium dioxide based photocatalysts could be synthesized in a single step by means of sonophotodeposition (SPD) methodology.[30–32] Herein, reducing agents are electrons produced as a result of UV absorption by a semiconducting material, whereas US assures enhanced mass transfer between reagents and helps in the reduction of the metal. The advantages of SPD methodology over conventional methods can include one-step synthesis, preparation at room temperature and atmospheric pressure, no need to use reducing agents, and very short reaction times. Furthermore, the physicochemical properties (high surface area and phase purity, particles with different sizes and shapes, uniform coating of nanoparticles on substrates, and many others) of the produced photocatalytic materials can be easily tuned by properly adjusting the parameters and conditions adopted in their preparation.

Herein, we describe an US-induced photodeposition procedure (SPD) for bimetallic photocatalyst synthesis (Pd–Au/TiO_2), along with their characterization and photocatalytic performances in the selective oxidation of methanol to form MF. To the best of our knowledge, this is the first study on the selective photocatalytic oxidation of methanol by using TiO_2 P90 modified on its surface with bimetallic Pd–Au nanoparticles prepared by SPD.

Results and Discussion

Photocatalyst characterization

In terms of photocatalyst specific surface areas (ca. 104 $m^2 g^{-1}$), pore volume (ca. 0.45 $mL g^{-1}$), and pore diameter (ca. 15 nm, mesoporous), all materials showed very similar textural features.

XRD measurements were performed to evaluate the structure of the bimetallic photocatalysts. Diffraction peaks of the bimetallic 1 wt% Pd–Au/TiO_2 photocatalysts (1 wt% Pd90–Au10/TiO_2, 1 wt% Pd75–Au25/TiO_2, and 1 wt% Pd50–Au50/TiO_2), monometallic 1 wt% Pd/TiO_2 P90 photocatalysts, and TiO_2 P90 are shown in Figure 1. For each photocatalyst shown in Table 1, the XRD data indicated that titania was mainly composed of anatase (ca. 84%) and rutile (ca. 16%) phases. The addition of noble metals and changes to the preparation conditions did not alter the phase composition of TiO_2. The average size of anatase and rutile crystallites for our photocatalysts, estimated by using the Scherrer equation, were about 13 and 25 nm, respectively. Additionally, from the XRD patterns, peaks of metallic gold ($2\theta = 38.2°$, 44.4°, 64.8°, and 77.9°) and metallic palladium ($2\theta = 40.1°$) were detected for all bimetallic photocatalysts. In addition, for the same bimetallic photocatalysts, the very broad diffraction peak of the palladium oxide phase (PdO: $2\theta = 34°$) was observed.[33–35] The crystallite sizes of gold in all bimetallic photocatalysts were approximately 11 nm and the crystallite sizes of palladium metal were twofold larger (ca. 20 nm) than those of palladium oxide (ca. 10 nm) for the photocatalysts prepared by SPD method (Table 1).

Table 1. Structural and optical properties of all tested photocatalysts prepared by the SPD method.

Photocatalyst	E_g [eV]	UV/Vis absorption threshold [nm]	XRD crystal phase[a] [%]	crystallite size [nm]	diameter [nm] Pd	PdO	Au
1 wt% Pd90–Au10/TiO_2 P90	2.43	510	A (84)	13	21	11	11
			R (16)	25			
1 wt% Pd75–Au25/TiO_2 P90	2.49	497	A (84)	13	21	11	13
			R (16)	30			
1 wt% Pd50–Au50/TiO_2 P90	2.55	486	A (84)	13	19	8	8
			R (16)	28			
1 wt% Pd/TiO_2 P90	2.51	493	A (74)	12	24	–	–
			R (26)	26			
TiO_2 P90	2.96	418	A (84)	12	–	–	–
			R (16)	23			

[a] A = anatase, R = rutile.

tems; this could be due to the absence of small Au and Pd clusters on the surface. This effect might be due to some gold and palladium nanoparticles starting to sinter and presenting larger particle sizes (Table 1), which would cause the wider absorption of light on the metallic surfaces.[38] The energy values (correlation coefficient $R^2 > 0.99$) corresponding to the forbidden energy (E_g) for each material were calculated and are reported in Table 1. The value for pure TiO_2 P90 was

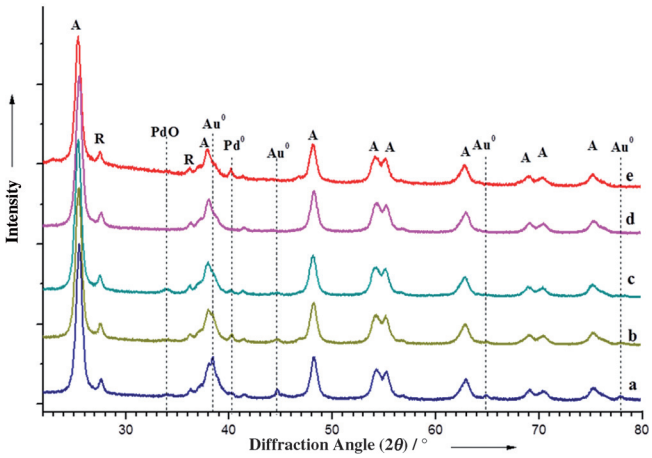

Figure 1. XRD patterns of different photocatalysts: a) 1 wt% Pd50–Au50/TiO_2, b) 1 wt% Pd75–Au25/TiO_2, c) 1 wt% Pd90–Au10/TiO_2, d) TiO_2 P90, and e) 1 wt% Pd/TiO_2 P90; *x* indicates the percentage of Pd or Au in the bimetallic nanoparticles, Pd*x*–Au*x*.

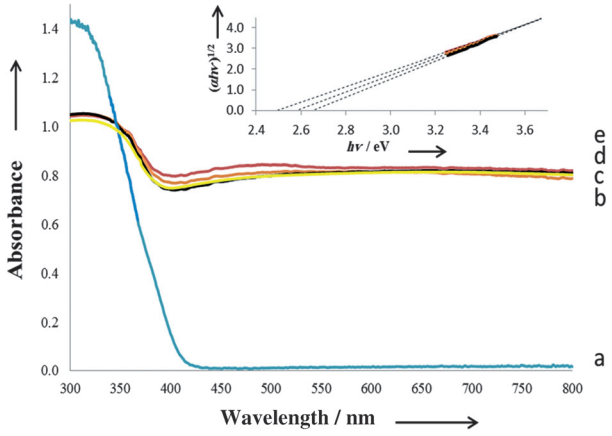

Figure 2. DR UV/Vis spectra of all tested photocatalysts: a) TiO_2 P90, b) 1 wt% Pd/TiO_2 P90, c) 1 wt% Pd90–Au10/TiO_2, d) 1 wt% Pd75–Au25/TiO_2, and e) 1 wt% Pd50–Au50/TiO_2. Inset: photocatalyst band gap, E_g, calculations.

The optical properties of the photocatalysts were studied by diffuse reflectance (DR) UV/Vis spectroscopy. Figure 2 depicts the DR spectra of all tested photocatalysts. The results obtained indicated that visible-light absorption of TiO_2 P90 prepared by the SPD method was significantly improved by introducing Au and Pd nanoparticles ($E_g \approx 2.5$ eV, absorption threshold $\lambda \approx 497$ nm; Table 1). The absorption band edge is strongly related to the Au and Pd nanoparticle size, shape, and Schottky barrier within the Pd–Au/TiO_2 interfaces in the photocatalyst samples. For sample 1 wt% Pd/TiO_2 P90, sharp absorbance edges occur at a wavelength of $\lambda \approx 493$ nm. For gold nanoparticles, an increase in the absorbance in the visible range from $\lambda = 486$ to 510 nm was observed. The interaction of light on the surface of the metallic nanoparticles produced the effect known as surface plasmon resonance (SPR) and a strong broad SPR absorption band is observed in the absorption spectra of many metallic nanoparticles, in particular, for gold.[36,37] However, no distinct SPR absorption peak over the entire spectral range could be detected for the monometallic 1 wt% Pd/TiO_2 P90 and bimetallic 1 wt% Pd–Au/TiO_2 P90 photocatalyst systems; this could be due to the absence of small Au and Pd clusters on the surface. This effect might be due to some gold and palladium nanoparticles starting to sinter and presenting larger particle sizes (Table 1), which would cause the wider absorption of light on the metallic surfaces.[38] The energy values (correlation coefficient $R^2 > 0.99$) corresponding to the forbidden energy (E_g) for each material were calculated and are reported in Table 1. The value for pure TiO_2 P90 was 2.96 eV, whereas the values for the materials containing Au and Pd on the surface were between 2.43 and 2.55 eV; this indicated that there was a slight displacement of the E_g of TiO_2 to lower energy values when Au and Pd particles were deposited on its surface. It has been reported by Kamat that the electrons can be transferred from excited TiO_2 to the metallic nanoparticles that work as cocatalysts until the two systems attain an equilibrium.[39] Electron accumulation increases the Fermi level of the nanoparticle to more negative potentials and the resultant Fermi level of the composite shifts closer to the conduction band (CB) of the semiconductor. Therefore, the involved edge energy E_g in electron transfer from TiO_2 to the metallic nanoparticles is lower than that of bare TiO_2 and the addition of Pd and Au leads to enhanced absorption of light in the visible region by TiO_2.

To gain more information about the surface composition and metal oxidation stages of the photocatalysts, all samples were studied by X-ray photoelectron spectroscopy (XPS). The binding energies (BEs) and atomic surface concentrations of all tested photocatalysts determined by XPS are given in Table 2.

Table 2. XPS results for all tested photocatalysts prepared by the SPD method.

Photocatalyst	Binding energy [eV] ([at %])					Atomic ratio	
	Au^0 ($4f_{7/2}$)	Pd^0 ($3d_{5/2}$)	PdO ($3d_{5/2}$)	Ti^{4+} ($2p_{3/2}$)	Ti^{3+} ($2p_{3/2}$)	Pd/Ti	Au/Ti
1 wt% Pd90–Au10/TiO_2P90	84.1 (0.05)	–	336.2 (0.07)	458.7 (22.67)	–	0.003	0.002
1 wt% Pd75–Au25/TiO_2P90	83.3(0.04)	334.3 (0.03)	336.2 (0.09)	458.6 (22.31)	–	0.005	0.002
1 wt% Pd50–Au50/TiO_2P90	82.9 (0.06)	334.1 (0.03)	336.0 (0.06)	458.6 (24.04)	457.0 (0.55)	0.004	0.003
1 wt% Pd/TiO_2P90	–	334.9 (0.06)	–	458.7 (23.12)	–	0.0024	–
TiO_2P90	–	–	–	458.8 (21.83)	–	–	–

The Pd 3d and Au 4f spectra for 1 wt% Pd75–Au25/TiO_2 P90 and 1 wt% Pd50–Au50/TiO_2 P90 show that the BEs of Pd^0 ($3d_{5/2}$ = 334.3 eV; 334.1 eV) and Au^0 ($4f_{7/2}$ = 83.3 eV; 82.9 eV) slightly deviate from the standard values of metallic Pd ($3d_{5/2}$ = 334.9 eV) and metallic Au ($4f_{7/2}$ = 84.0 eV).[33–35] With increasing gold loading, the Pd^0 $3d_{5/2}$ and Au^0 $4f_{7/2}$ XPS peaks are found to shift to lower BEs, which further confirms the formation of the Pd–Au alloy. This observed small shift to lower BEs could be attributed to electron exchange between the Pd and Au nanoparticles,[40] and/or synergistic interactions between TiO_2 and noble-metal nanoparticles (SMSI effect).[41–43] Also, for these photocatalysts and 1 wt% Pd90–Au10/TiO_2 P90, the BEs of Pd $3d_{5/2}$ were detected at 336.0–336.2 eV, which could be attributed to the presence of Pd in the form of PdO. Some researchers described that the lower BE value of Pd 3d might have been due to the increase in charge density in the d band, concomitant with loss in the sp band; this suggests more pronounced Au–Pd bond formation on the surface of Pd–Au nanoparticles,[36] especially for 1 wt% Pd50–Au50/TiO_2 P90 (the most active/selective material in methanol oxidation) for which we detected the highest Pd and Au shift to lower BEs and also the formation of Ti^{3+} ions on the photocatalyst surface (Table 2). We have evidence to believe that $[(Pd)_n^{\sigma-}–(Au)_n^{\sigma-}]/[Ti^{3+}]$ species may have a strong influence on such good activity and selectivity observed for this photocatalytic system. Xu et al. reported a −0.4 eV shift for Au 4f and a −0.1 eV shift for the Pd 3d peak in Pd–Au/SiO_2,[44] and Hsu et al. observed a −0.5 eV shift for the Pd $3d_{5/2}$ peak in the Pd–Au core–shell nanoparticle.[45] For 1 wt% Pd90–Au10/TiO_2 P90 in the Pd 3d region, Pd^0 species were not identified. The 1 wt% Pd50–Au50/TiO_2 P90 sample exhibited a broader peak with an additional shoulder at a lower BE (456.98 eV) relative to that of bare TiO_2 P90. The Ti $2p_{3/2}$ spectra could be fitted with a dominant peak centered at 458.6 eV and a lower BE of 457.0 eV. The former was associated with Ti ions with a formal valence of four (Ti^{4+}), whereas the latter was associated with Ti ions with a reduced charge state (Ti^{3+}).[46,47] The increased signal at 457.0 eV for 1 wt% Pd50–Au50/TiO_2 P90, corresponding to Ti^{3+}, could be caused by chemical reduction from Ti^{4+} to Ti^{3+} during synthesis of the photocatalyst.

To obtain more evidence regarding the nature of the deposited palladium and gold particles, high-resolution transmission electron microscopy (HRTEM) measurements were employed. Selected micrographs of Pd–Au/TiO_2 and Pd/TiO_2 samples are shown in Figure 3. As observed in Figure 3 a–c, in each system, palladium and gold particles mostly form spherically shaped agglomerations with diameter from about 12 to 100 nm. The formation of these aggregates could be ascribed to the preparation technique used for samples in the HRTEM measurements. From the average particle size of TiO_2 P90, about 12 nm based on XRD measurements, the tendency to form aggregates is natural. Therefore, the Pd–Au/TiO_2 and Pd/TiO_2 particles could agglomerate during alcohol evaporation before HRTEM analysis. The close proximity of metal nanoparticles is evidenced by HRTEM (Figure 4 a).

The HRTEM image and EDS spectrum (Figure 4) were recorded to obtain information on the size, shape, and elemental analysis of the metal particles of 1 wt% Pd50–Au50/TiO_2 P90 as the most selective photocatalyst. In this case, the EDS pattern confirmed the successful deposition of Pd and Au particles on the TiO_2 surface by applying the SPD method, and also indicated the presence of both noble metals in close proximity and with the planned nominal (50:50 = 1:1 atomic ratio) noble-metal composition for 1 wt% Pd50–Au50/TiO_2 P90.

Photocatalytic activity and stability

Photocatalytic oxidation of methanol in gas phase was chosen as the test reaction to evaluate the photocatalytic properties of all prepared materials. After 2 h of light irradiation, CO_2 and MF were identified as the only two reaction products, according to Equations (1) and (2):

$$2\,CH_3OH + 3\,O_2 \rightarrow 2\,CO_2 + 4\,H_2O \quad (1)$$

$$2\,CH_3OH + O_2 \rightarrow HCOOCH_3 + H_2O \quad (2)$$

Initially, three control experiments were applied: 1) photolysis upon UV illumination in the presence of pollutant in the air flow and without photocatalyst, 2) photocatalytic methanol oxidation in the presence of the 1 wt% Pd50–Au50/TiO_2 photocatalyst without oxygen (argon instead of air), and 3) the thermal effect (up to 100 °C) in the dark, in the presence of the photocatalyst and pollutant in the air flow. Additionally, for the best performing photocatalyst (1 wt% Pd50–Au50/TiO_2 P90), temperature-programmed oxidation (TPO) of coke deposited on its surface after 2 h of photocatalysis was conducted (Figure 5.

In the photolysis experiment (absence of photocatalyst), very low conversion of methanol (< 3%) was observed; thus confirming that the photodegradation reaction was really enabled by a photocatalytic process. Moreover, the catalyst was not active under the thermal conditions (up to 100 °C) in the dark. Therefore, we conclude that this reaction depends on the presence of both light and a photocatalyst.

In the absence of oxygen (air), the 1 wt% Pd50–Au50/TiO_2 P90 photocatalyst exhibited extremely low methanol conversion (< 5%), good stability with the time of the stream, and the highest selectivity to MF (80%; Figures 6 and 8 below). As

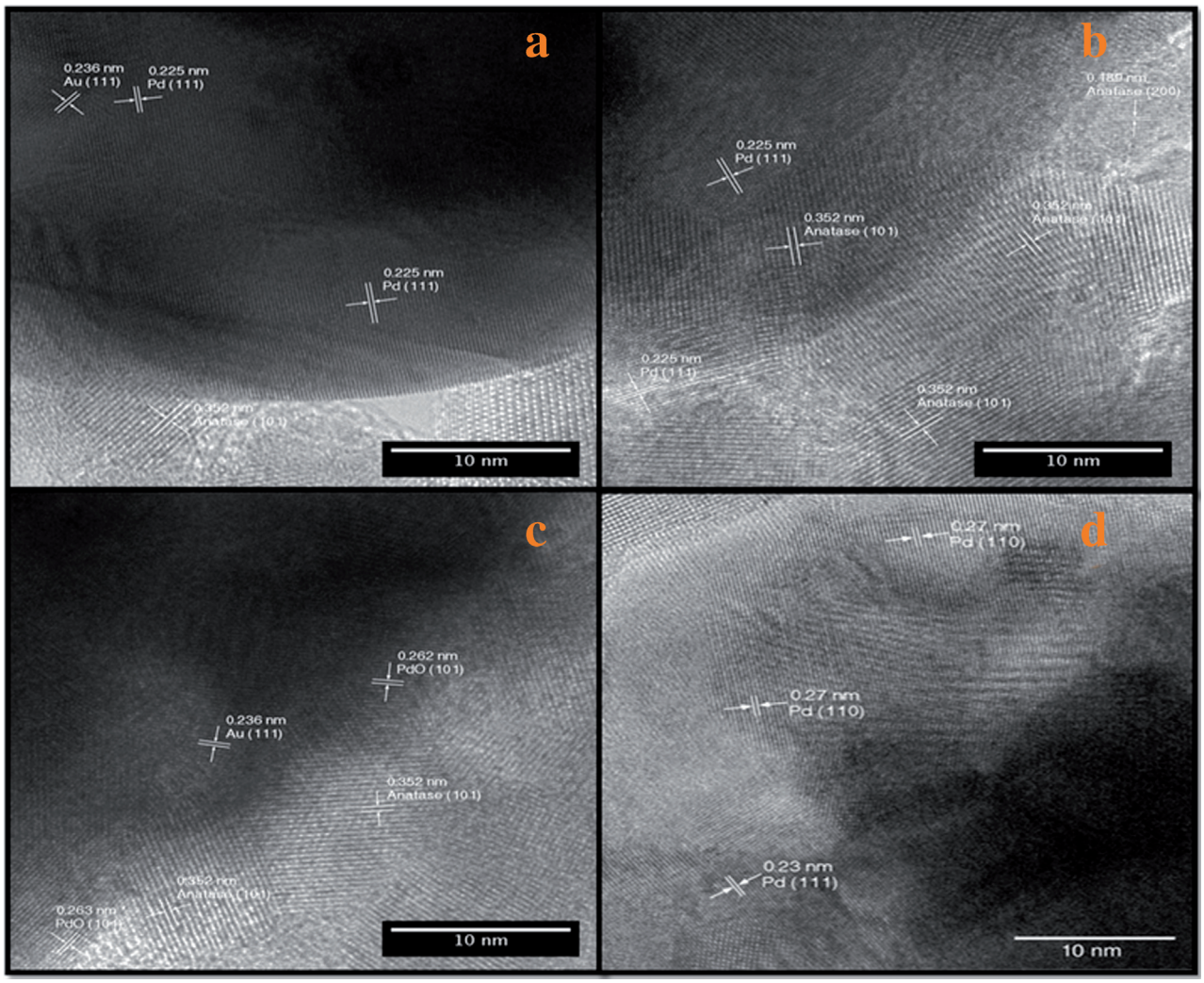

Figure 3. HRTEM images of photocatalysts a) 1 wt% Pd90–Au10/TiO_2 P90, b) 1 wt% Pd75–Au25/TiO_2 P90, c) 1 wt% Pd50–Au50/TiO_2 P90, and d) 1 wt% Pd/TiO_2 P90.

we can see in Figure 6, the presence of oxygen (air) is extremely important to improve the activity of the photocatalysts, especially for bimetallic systems. We believe that in the absence of oxygen (air) selective oxidation takes place through TiO_2 (in 1 wt% Pd50–Au50/TiO_2 P90) lattice oxygen atoms, and that oxygen (supplied in air flow) is needed only to replenish the oxygen vacancies produced on the TiO_2 lattice. When gas-phase oxygen was present, the oxidation rate of methanol was greatly improved (Figure 6); this suggested the important role of adsorbed oxygen.

The TPO experiment was used to measure the amount of "organic residues" potentially remaining on the surface of the best performing photocatalyst (1 wt% Pd50–Au50/TiO_2 P90) after the reaction. After 2 h of light irradiation, the 1 wt% Pd50–Au50/TiO_2P90 photocatalyst was heated first at 100 °C for 2 h in a 25 mL min^{-1} flow of helium to remove all physisorbed reagents and products from the photocatalyst surface, and then the photocatalyst was cooled to room temperature, from which temperature a heating ramp rate of 10 °C min^{-1} was used up to 500 °C in a 25 mL min^{-1} flow of air, and GC online analysis of CO_2 (oxidation product) was monitored (Figure 5). This TPO experiment showed the presence of carbon deposits on the surface of the photocatalysts in less than 0.1% of the total amount of methanol feed after 2 h of photocatalysis; this provided us with the whole carbon balance after photocatalytic methanol oxidation and confirmed the high stability of 1 wt% Pd50–Au50/TiO_2P90 in the selective oxidation of methanol to form MF.

Figure 6 displays the photocatalytic conversion of methanol over monometallic 1 wt% Pd/TiO_2 P90 and bimetallic 1 wt% Pd–Au/TiO_2 P90 photocatalysts as a function of light irradiation time, together with that of the TiO_2 P90 photocatalyst for comparison. It is clearly seen that modification of TiO_2 with Pd and Au through the SPD method results in a great enhancement of photocatalytic activity. Titania itself was only active (ca. 33% methanol conversion; Figure 6) towards the total oxidation of methanol to form carbon dioxide under UV irradiation. It should be noted that the 1 wt% Pd/TiO_2 P90 sample exhibited the highest methanol conversion of all tested photocatalysts, but without MF production and with the highest grade of

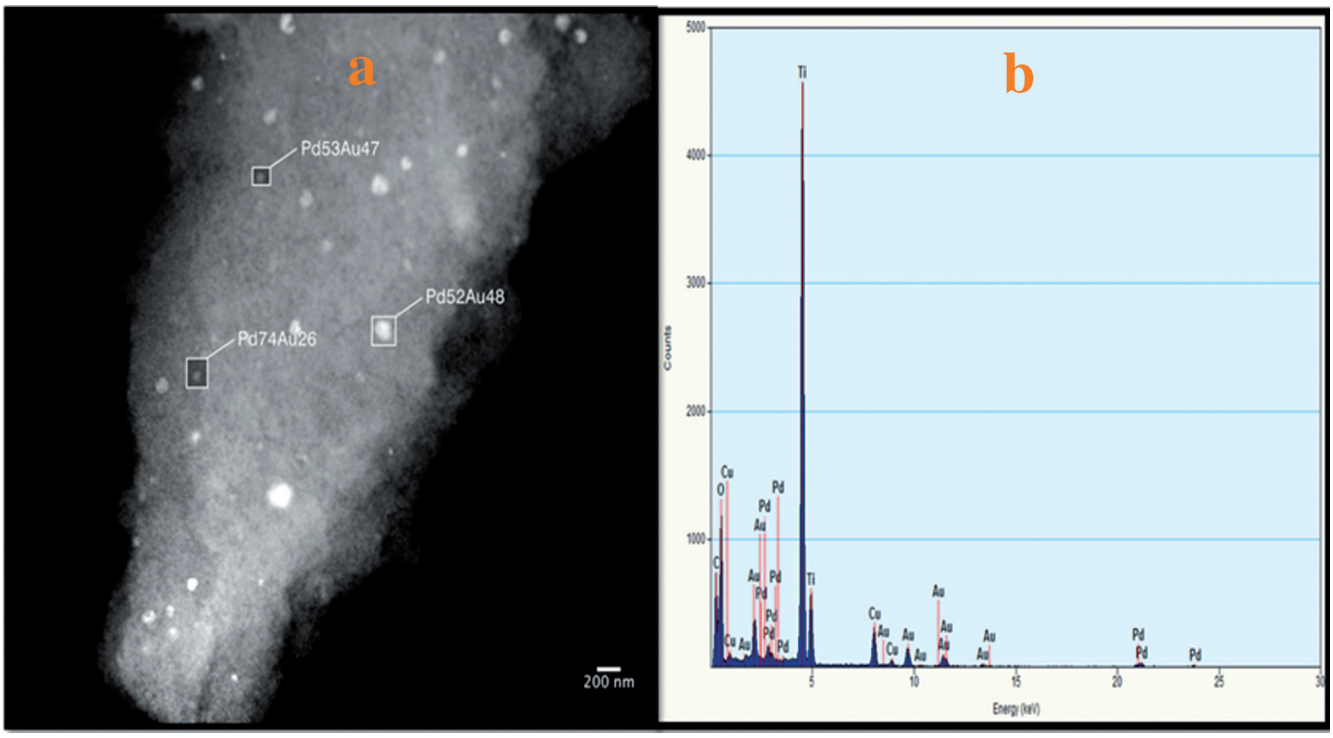

Figure 4. a) HRTEM image and b) energy-dispersion X-ray spectroscopy (EDS) results for the 1 wt% Pd50–Au50/TiO_2 P90 photocatalyst.

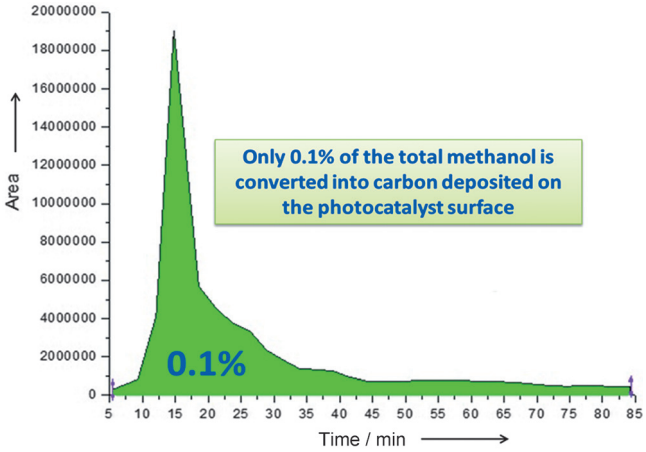

Figure 5. TPO experiment of carbon deposited on 1 wt% Pd50–Au50/TiO_2P90 photocatalyst surface after 120 min of photocatalysis.

total mineralization (83%; Figure 7) after 2 h of light irradiation. Among all tested materials, the best selectivity (70%; Figure 8) to MF (with very good methanol conversion of 85%; Figure 6) was obtained for 1 wt% Pd50–Au50/TiO_2P90 prepared by the SPD method as a function of light irradiation. It was also observed that photocatalysts containing Pd–Au nanoparticles supported on TiO_2 P90 exhibited a much lower mineralization rate to carbon dioxide under the applied reaction conditions (Figure 7). Furthermore, we obtained inferior results for the 1 wt% Pd50–Au50/TiO_2P90/PD photocatalyst prepared by only the photodeposition method (2 h of illumination, resulted in a methanol conversion of 59%, which was slightly deactivated after 80 min of photocatalysis, and in a selectivity to MF of 38% and to CO_2 of 62%). This control experiment showed a significant advantage of SPD over the photodeposition method in the preparation of materials with photocatalytic properties for selective oxidation reactions.

The addition of Au dramatically improved the selectivity to MF (>70%) in the monometallic Pd/TiO_2 system, with a slight decrease in methanol conversion. In contrast, 1% Pd/TiO_2 P90 and TiO_2 P90 are inactive in the selective methanol oxidation to form MF, but are active and selective for CO_2 formation. Such results suggest the advantages of the bimetallic Pd–Au catalysts over the monometallic catalyst in selective methanol conversion. The combination of Au with Pd (Pd–Au bimetallic photocatalyst) significantly enhanced both the photocatalytic activity and selectivity towards MF, which suggested a synergistic interaction between Au and Pd, and also the SMSI of TiO_2 and Pd–Au further strengthened the coordination effect of Au and Pd.[41–43] The addition of cocatalytic amounts of Au to Pd markedly enhanced the selectivity of supported Pd–Au due to the electronic effect, as confirmed by UV/Vis spectroscopy and XPS. The results obtained indicated that the size and amount of noble metal at the surface of TiO_2 affected their near-UV light-induced photoactivity. Similarly, the strong influence of the TiO_2 support on the visible-light-induced activity of Au-modified TiO_2 particles was observed by Kowalska et al. for the photocatalytic dehydrogenation of methanol.[48] They suggested that titania particles could influence the reaction rate directly and indirectly. The direct effect was due to the properties of titania, such as size, shape, aggregation, surface defects, and CB position, whereas the indirect effect was due to titania–gold interactions, such as complex energetic properties (electron mobility), as well as the impact of titania on the proper-

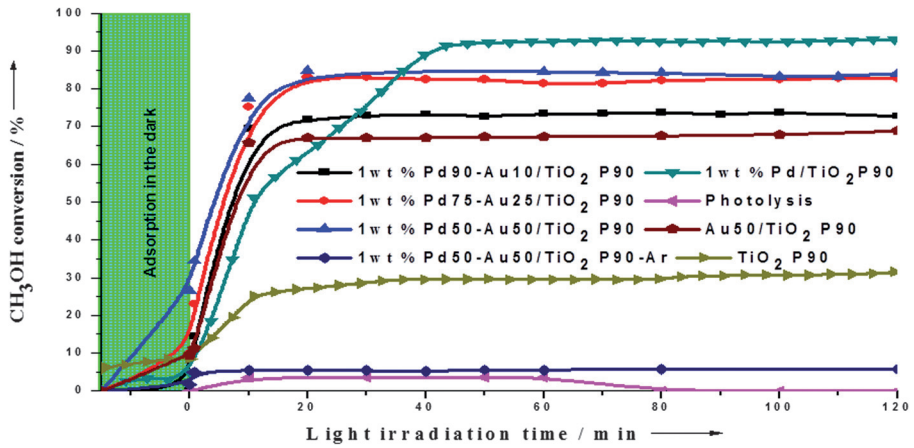

Figure 6. Profiles of photocatalytic methanol conversion as a function of light irradiation time over all tested photocatalysts.

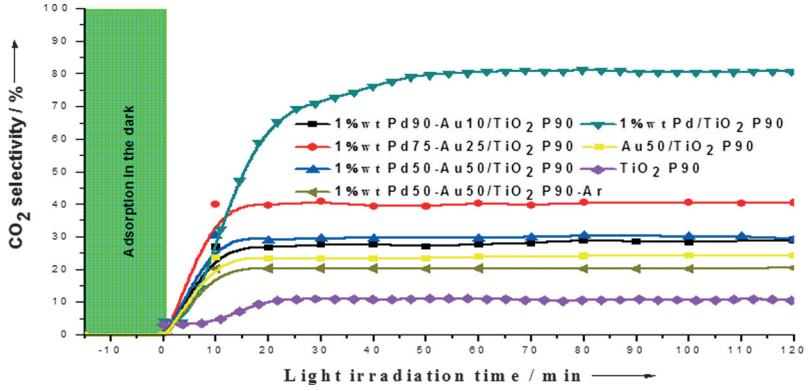

Figure 7. Selectivity to carbon dioxide as a function of light irradiation time over all tested photocatalysts.

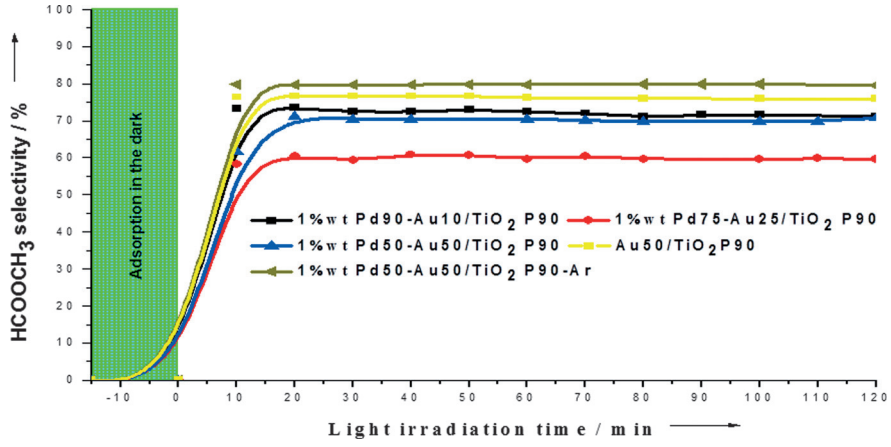

Figure 8. Selectivity to MF as a function of light irradiation time over all tested photocatalysts.

ties of generated gold, such as a size, shape, stability, and (in)-activation.[48]

The incorporation of noble metals with a large work function (e.g., Au, Pd in the shape of Pd–Au metal nanoparticle random alloys) onto a TiO_2 support has been shown to significantly enhance the charge-separation efficiency (a decrease in the recombination rate of photogenerated charges) through interfacial electron transfer from the CB of TiO_2 to metals on the surface. Increasing the lifetime of the charges will increase their chances of diffusing to the surface and participating in the photocatalytic process to promote the reduction half-reaction (oxygen reduction) that is considered to be the rate-limiting step in photocatalysis. As one can see, the high selectivity to MF depends on the amount, oxidation state of the metals, and their interfacial behavior on the titania surface. As observed by XPS measurements for 1 wt% Pd50–Au50/TiO_2 P90, the SMSI effect can have an important role in the selective oxidation of methanol. To the best of our knowledge, this is the first report on the formation of such an effect (SMSI = $[(Pd)_n^{\sigma-}$–$(Au)_n^{\sigma-}]/[Ti^{3+}]$) by the influence of US. This effect is believed to occur during synthesis of the photocatalyst due to shock waves and interparticle collision caused by acoustic cavitation. In such a specific environment, the Pd–Au↔TiO_2 strong interactions are probable, especially after optimization of one of the most important parameters, such as the appropriate composition of metals, as observed for the best performing photocatalyst, 1 wt% Pd50–Au50/TiO_2 P90, but this hypothesis needs more research to be undeniably proven.

Conclusions

A simple photodeposition method coupled with ultrasonic irradiation (sonophotodeposition (SPD) method) can be successfully used for the preparation of Pd–Au alloy nanoparticles supported on titania with high activity (83%), selectivity (70%), and stability (with very low carbon formation on the catalyst surface, 0.1% after 120 min of reaction) in the selective oxidative esterification of methanol to MF. We strongly believe that the strong metal–support interaction effect (SMSI) between Pd–Au alloy nanoparticles and the TiO_2

surface is one of the reasons for such good activity and selectivity for the best performing photocatalyst (1 wt% Pd50–Au50/TiO_2 P90).

This synthetic procedure for the preparation of the photocatalysts is highly energy efficient and reactions can be carried out under mild conditions (room temperature and atmospheric pressure), in short times, and without using strong chemical reducing agents.

These results not only greatly broaden and deepen the fundamental understanding of the photochemistry of methanol on the Pd–Au/TiO_2 surface, but also demonstrate a novel, green, benign, and sustainable photocatalytic route for the synthesis of esters directly from alcohols.

Experimental Section

Photocatalyst preparation

Palladium(II) acetylacetonate (Acros), hydrogen tetrachloroaurate(III) trihydrate (Alfa Aesar), and commercial TiO_2 (AEROXIDE TiO_2 P90, Evonik Industries) were used as the Pd precursor, Au precursor, and TiO_2 support, respectively. The detailed procedure was as follows: oxalic acid (0.1 g) and desired amounts of Pd and Au precursors were dissolved in H_2O/CH_3CN (120 mL; 30:70, v/v) and TiO_2 (0.5 g) was dispersed into this solution and the pH was adjusted to about 2. The nominal palladium loading for all bimetallic photocatalysts was designed to be 1.0 wt% (0.05 mmol) with different atom content Pd/Au ratios of 90:10, 75:25, and 50:50. The batch photoreactor with such a prepared mixture was placed into the ultrasonic bath (35 kHz, 560 W, Sonorex Digitec-RC, Bandelin; Figure 9b). The suspension was first kept in the dark for 30 min to reach complete adsorption equilibrium. SPD was performed by illuminating the suspension for 60 min with a low-pressure mercury lamp (6 W, $\lambda_{max} = 254$ nm) and the ultrasonic bath switched on. The synthesis reaction was carried out under a flow of argon (flow rate: 70 mL min^{-1}) and thermostated at 20 °C. Next, the product was recovered by slow evaporation on a rotary evaporator, repeated filtering, and washing three times with Millipore water until a negative test for chloride ions could be detected by adding a solution of $AgNO_3$ (0.1 mol L^{-1}) to the filtrate (only the photocatalysts containing gold). Then, the samples were dried at 110 °C for 10 h, and calcined at 300 °C for 4 h under a flow of air (flow rate 30 mL min^{-1}). The photocatalysts were labelled as 1 wt% Pd90–Au10/TiO_2 P90, 1 wt% Pd75–Au25/TiO_2 P90, and 1 wt% Pd50–Au50/TiO_2 P90. For comparative purposes, 1 wt% Pd/TiO_2 P90 and Au50/TiO_2 P90 were prepared by the SPD method, and 1 wt% Pd50-Au50/TiO_2 P90 was synthesized by photodeposition (without US). Unmodified TiO_2 P90 was chosen as a reference material, without the addition of metal precursors.

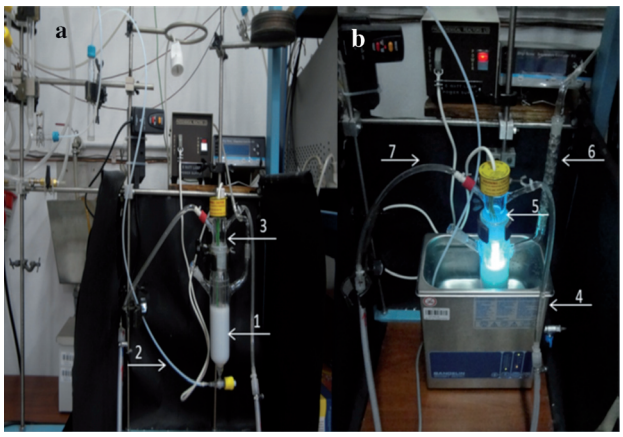

Figure 9. SPD reaction setup before (a) and during the reaction (b): 1) batch photoreactor, 2) argon line, 3) switched off 6 W UV lamp, 4) ultrasonic bath, 5) switched on 6 W UV lamp, 6) reflux condenser, and 7) lamp cooling system (20 °C).

Photocatalytic activity measurements

A schematic representation of the methanol photo-oxidation setup is given in Figure 10.[32] Methanol was introduced by bubbling air

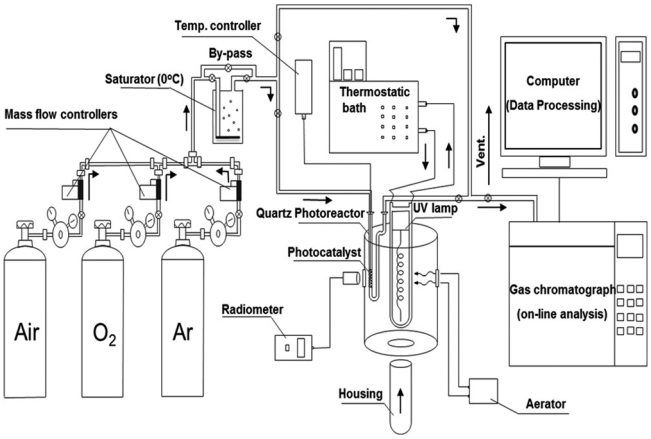

Figure 10. Schematic representation of the methanol photo-oxidation system.

(25 cm^3 min^{-1}) through a glass saturator filled with methanol. The saturator was immersed in a thermostat maintained at 0 °C. The gas flow rates were measured and controlled by mass flow controllers (supplied by Bronkhorst HI-TEC). The flow-type photoreactor was vertically enclosed by an aluminum foil cylindrical reflector (20 cm × 13 cm × 1 mm) to exclude any external light source and maximize light energy usage within the reactor. The photocatalyst bed height was 5 cm. The adsorption equilibrium reagent photocatalyst was achieved in the dark after 2 h. The light source was a medium-pressure 125 W mercury lamp ($\lambda_{max} = 365$ nm; supplied by Photochemical Reactors Ltd. Model RQ3010) built into a lamp housing and centered vertically in the reflector (2.5 cm between the lamp and photoreactor) and thermostated at 30 °C. The average luminous intensity (≈260 mW cm^{-2}) was determined by means of a radiometer ILT 1400 (supplied by International Light Technologies, Inc., USA) with a UV/Vis laser power probe ($\lambda = 250$–675 nm). Reaction products were quantitatively analyzed by means of an online gas chromatography (HP 5890 series II Hewlett Packard USA equipped with a flame ionization detector (FID) and a methanizer model 510 instrument supplied by SRI INSTRUMENTS) and identified offline by GC–MS (HP-5 column GC (6890 Series)–MS(5973) Hewlett Packard equipped with FID and thermal conductivity detector (TCD)).

Characterization methods

The specific surface area, pore volume, and average pore diameter were determined by N_2 physisorption by using a Micromeritics ASAP 2020 automated system and the Brunauer–Emmet–Teller

(BET)[49] and the Barret–Joyner–Halenda (BJH) methods.[50] Each photocatalyst was degassed under vacuum at $<1\times10^{-5}$ bar in the Micromeritics system at 300 °C for 4 h prior to N_2 physisorption.

Powder XRD measurements were performed by using the standard Bragg–Brentano configuration. This type of arrangement was provided by using a Siemens D5000 diffractometer (equipped with a horizontal goniometer) with θ–2θ geometry and Ni-filtered CuK_α radiation, powered at 40 kV and 40 mA. Data were collected in the range of $2\theta = 10$–$90°$ with a step interval of 0.02° and counting time of up to 5 s per step.

The average crystallite size (D in nm) was determined according to the Scherrer equation [Eq. (3)]:[51]

$$D = \frac{k\lambda}{\beta\cos\theta} \tag{3}$$

in which D is the average crystallite size of the catalyst (nm), λ is the wavelength of the CuK_λ X-ray radiation ($\lambda = 0.154056$ nm), k is a coefficient usually taken as 0.94, β is the full-width at half-maximum (FWHM) intensity of the peak observed at 2θ (radian), and θ is the diffraction angle. The phase contents of the samples could be estimated from the respective XRD peak intensities by using Equation (4):[52]

$$\begin{aligned} f_A &= \frac{1}{1+\frac{1}{k}\frac{I_R}{I_A}} \\ k &= 0.79 \;\; f_A > 0.2 \\ k &= 0.68 \;\; f_A \le 0.2 \end{aligned} \tag{4}$$

in which f_A is the fraction of anatase phase in the powder, and I_A and I_R are the X-ray intensities of the anatase (101) and rutile (110) diffraction peaks, respectively.

HRTEM measurements were carried out by using an FEI TITAN Cubed electron microscope operated at an acceleration voltage of 300 keV and equipped with an EDS EDAX spectrometer. The samples were prepared as a dispersion in pure alcohol by using an ultrasonic cleaner and putting a drop of this suspension on carbon films on copper grids that were purified with plasma cleaner.

The XPS measurements were performed by using a VG Scientific photoelectron spectrometer ESCALAB-210 with AlK_α radiation (1486.6 eV) from an X-ray source operating at 15 kV and 20 mA. Survey spectra were recorded for all samples in the energy range from 0 to 1350 eV with a 0.4 eV step. High-resolution spectra were recorded with a 0.1 eV step, 100 ms dwell time, and 25 eV pass energy. A take-off angle of 60° was used in all measurements. Curve fitting was performed by using the AVANTAGE software provided by Thermo Electron, which described each component of the complex envelope as a Gaussian–Lorentzian (G/L) sum function; a constant 0.3(±0.05) G/L ratio was used. The background was fitted by using a nonlinear Shirley model. Scofield sensitivity factors and a measured transmission function were used for quantification. The aromatic carbon C 1s peak at 284.5 eV was used as a BE reference.

DR UV/Vis spectroscopy was performed by using a UV/Vis/NIR Jasco V-570 spectrophotometer equipped with an integrating sphere. The baseline was recorded by using Spectralon [poly(tetrafluoroethylene)] as a reference material. Band gap values were calculated based on the Kubelka–Munk functions,[53] $f(R)$, which were proportional to the absorption of radiation, by plotting $[f(R)h\nu)]^{1/2}$ against $h\nu$. The function $f(R)$ was calculated by using Equation (5):

$$f(R) = \frac{(1-R)^2}{2R} \tag{5}$$

Band gap values were obtained from the plot of the Kubelka–Munk function $[F(R_\infty)E]^{1/2}$ versus the energy of the absorbed light, E. The absorption threshold was determined by using Equation (6):[54]

$$\lambda = \frac{1240}{E_g} \tag{6}$$

Acknowledgements

This work was supported by the National Science Centre (NCN) in Poland within research project DEC-2011/01/B/ST5/03888.

Keywords: gold · nanoparticles · oxidation · palladium · sonophotodeposition

[1] R. Marschall, *Adv. Funct. Mater.* **2014**, *24*, 2421 – 2440.
[2] T. Baran, W. Macyk, *J. Photochem. Photobiol. A* **2012**, *241*, 8 – 12.
[3] F. Fresno, R. Portela, S. Suarezc, J. M. Coronado, *J. Mater. Chem. A* **2014**, *2*, 2863 – 2884.
[4] M. Pelaez, N. T. Nolan, S. C. Pillai, M. K. Seery, P. Falaras, A. G. Kontos, P. S. M. Dunlop, J. W. J. Hamilton, J. A. Byrne, K. O'Shea, M. H. Entezari, D. D. Dionysiou, *Appl. Catal. B* **2012**, *125*, 331 – 349.
[5] J. C. Colmenares, R. Luque, *Chem. Soc. Rev.* **2014**, *43*, 765 – 778.
[6] J. Zhang, A. N. Alexandrova, *J. Phys. Chem. Lett.* **2013**, *4*, 2250 – 2255.
[7] T. Ward, L. Delannoy, R. Hahn, S. Kendell, C. J. Pursell, C. Louis, B. D. Chandler, *ACS Catal.* **2013**, *3*, 2644 – 2653.
[8] E. Kowalska, M. Janczarek, L. Rosac, S. Juodkazis, B. Ohtani, *Catal. Today* **2014**, *230*, 131 – 137.
[9] M. Sankar, N. Dimitratos, P. J. Miedziak, P. P. Wells, C. J. Kiely, G. J. Hutchings, *Chem. Soc. Rev.* **2012**, *41*, 8099 – 8139.
[10] J. C. Colmenares, *ChemSusChem* **2014**, *7*, 1512 – 1527.
[11] S. Scirè, L. F. Liotta, *Appl. Catal. B* **2012**, *125*, 222 – 246.
[12] S. Sakthivel, M. V. Shankar, M. Palanichamy, B. Arabindoo, D. W. Bahnemann, V. Murugesan, *Water Res.* **2004**, *38*, 3001 – 3008.
[13] V. Iliev, D. Tomova, R. Todorovska, D. Oliver, L. Petrov, D. Todorovsky, M. Uzunova-Bujnova, *Appl. Catal. A* **2006**, *313*, 115 – 121.
[14] K. Ralphs, Ch. Hardacre, S. L. James, *Chem. Soc. Rev.* **2013**, *42*, 7701 – 7718.
[15] Y. Z. Yang, C. H. Chang, H. Idriss, *Appl. Catal. B* **2006**, *67*, 217 – 222.
[16] C. H. Christensen, J. K. Nørskov, *Science* **2010**, *327*, 278 – 279.
[17] M. R. Buck, J. F. Bondi, R. E. Schaak, *Nat. Chem.* **2012**, *4*, 37 – 44.
[18] S. J. Freakley, M. Piccinini, J. K. Edwards, E. N. Ntainjua, J. A. Moulijn, G. J. Hutchings, *ACS Catal.* **2013**, *3*, 487 – 501.
[19] G. Jenner, *Appl. Catal. A* **1995**, *121*, 25 – 44.
[20] P. Rodriguez, Y. Kwon, M. T. M. Koper, *Nat. Chem.* **2012**, *4*, 177 – 182.
[21] G. Palmisano, E. Garcia-Lopez, G. Marci, V. Loddo, S. Yurdakal, V. Augugliaro, L. Palmisano, *Chem. Commun.* **2010**, *46*, 7074 – 7089.
[22] Z. Guo, B. Liu, Q. Zhang, W. Deng, Y. Wang, Y. Yang, *Chem. Soc. Rev.* **2014**, *43*, 3480 – 3524.
[23] W. Reutemann, H. Kieczka, *Ullmann's Encyclopedia of Industrial Chemistry, 7th ed.*, Wiley, Hoboken, **1999** – **2011**; entry on formic acid.
[24] H. Kominami, H. Sugahara, K. Hashimoto, *Catal. Commun.* **2010**, *11*, 426 – 429.
[25] Q. Guo, C. Xu, W. Yang, Z. Ren, Z. Ma, D. Dai, T. K. Minton, X. Yang, *J. Phys. Chem. C* **2013**, *117*, 5293 – 5300.
[26] K. R. Phillips, S. C. Jensen, M. Baron, S.-C. Li, C. M. Friend, *J. Am. Chem. Soc.* **2013**, *135*, 574 – 577.
[27] C. Han, X. Yang, G. Gao, J. Wang, H. Lu, J. Liu, M. Tong, X. Liang, *Green Chem.* **2014**, *16*, 3603 – 3615.
[28] J. H. Bang, K. S. Suslick, *Adv. Mater.* **2010**, *22*, 1039 – 1059.
[29] C. Kan, W. Cai, C. Li, L. Zhang, H. Hofmeister, *J. Phys. D* **2003**, *36*, 1609 – 1614.

[30] J. C. Colmenares, A. Magdziarz, *Polish Patent Application*, P-401693, **2012**.
[31] J. C. Colmenares, A. Magdziarz, D. Łomot, O. Chernyayeva, D. Lisovytskiy, *Appl. Catal. B* **2014**, *147*, 624 – 632.
[32] J. C. Colmenares, P. Lisowski, *Polish Patent Application*, P-405094, **2013**.
[33] B. Pongthawornsakuna, S. Fujita, M. Araib, O. Mekasuwandumrongc, J. Panpranota, *Appl. Catal. A* **2013**, *467*, 132 – 141.
[34] A. Cybula, J. B. Priebe, M.-M. Pohl, J. W. Sobczak, M. Schneider, A. Zielinska-Jurek, A. Brückner, A. Zaleska, *Appl. Catal. B* **2014**, *152 – 153*, 202 – 211.
[35] L. Ouyang, G. Da, P. Tian, T. Chen, G. Liang, J. Xu, Y.-F. Han, *J. Catal.* **2014**, *311*, 129 – 136.
[36] S. Naya, A. Inoue, H. Tada, *ChemPhysChem* **2011**, *12*, 2719 – 2723.
[37] F. Moreau, G. C. Bond, A. O. Taylor, *J. Catal.* **2005**, *231*, 105 – 114.
[38] S. Eustis, M. A. El-Sayed, *Chem. Soc. Rev.* **2006**, *35*, 209 – 217.
[39] P. V. Kamat, *J. Phys. Chem. B* **2002**, *106*, 7729 – 7744.
[40] R. Liu, Y. Yu, K. Yoshida, G. Li, H. Jiang, M. Zhang, F. Zhao, S. Fujita, M. Arai, *J. Catal.* **2010**, *269*, 191 – 200.
[41] M. Bowker, P. Stone, P. Morrall, R. Smith, R. Bennett, N. Perkins, R. Kvon, C. Pang, E. Fourre, M. Hall, *J. Catal.* **2005**, *234*, 172 – 181.
[42] D. W. Goodman, *Catal. Lett.* **2005**, *99*, 1 – 2.
[43] F. Solymosi, *Catal. Rev.* **1968**, *1*, 233 – 255.
[44] B. Xu, X. Liu, J. Haubrich, R. J. Madix, C. M. Friend, *Angew. Chem. Int. Ed.* **2009**, *48*, 4206 – 4209; *Angew. Chem.* **2009**, *121*, 4270 – 4273.
[45] C. Hsu, C. Huang, Y. Hao, F. Liu, *Electrochem. Commun.* **2012**, *23*, 133 – 136.
[46] L.-B. Xiong, J.-L. Li, B. Yang, Y. Yu, *J. Nanomater.* **2012**, 831524.
[47] X. Pan, M.-Q. Yang, X. Fu, N. Zhang, Y.-J. Xu, *Nanoscale* **2013**, *5*, 3601 – 3614.
[48] E. Kowalska, O. Prieto Mahaney, R. Abe, B. Ohtani, *Phys. Chem. Chem. Phys.* **2010**, *12*, 2344 – 2355.
[49] S. Brunauer, P. H. Emmett, E. Teller, *J. Am. Chem. Soc.* **1938**, *60*, 309 – 319.
[50] E. P. Barrett, L. G. Joyner, P. P. Halenda, *J. Am. Chem. Soc.* **1951**, *73*, 373 – 380.
[51] B. D. Cullity, S. R. Stock, *Elements of X-ray Diffraction, 3rd ed.*, Prentice Hall, Upper Saddle River, NJ, **2001**.
[52] R. A. Spurr, H. Myers, *Anal. Chem.* **1957**, *29*, 760 – 762.
[53] S. Sakthivel, H. Kisch, *Angew. Chem. Int. Ed.* **2003**, *42*, 4908 – 4911; *Angew. Chem.* **2003**, *115*, 5057 – 5060.
[54] H.-S. Lee, C.-S. Woo, B.-K. Youn, S.-Y. Kim, S.-T. Oh, Y.-E. Sung, H.-I. Lee, *Top. Catal.* **2005**, *35*, 255 – 260.

Received: October 14, 2014
Revised: November 25, 2014
Published online on February 11, 2015